Since January 2020 Elsevier has created a COVID-19 resource centre with free information in English and Mandarin on the novel coronavirus COVID-19. The COVID-19 resource centre is hosted on Elsevier Connect, the company's public news and information website.

Journal of the Taiwan Institute of Chemical Engineers 139 (2022) 104538

Contents lists available at ScienceDirect

Journal of the Taiwan Institute of Chemical Engineers

journal homepage: www.journals.elsevier.com/journal-of-the-taiwan-institute-of-chemical-engineers

Thermal degradation of hazardous 3-layered COVID-19 face mask through pyrolysis: Kinetic, thermodynamic, prediction modelling using ANN and volatile product characterization

Ahmad Nawaz *, Pradeep Kumar *

Department of Chemical Engineering and Technology, Indian Institute of Technology (BHU), Varanasi 221005, India

ARTICLE INFO

Keywords:
Pyrolysis
Three-layered face mask
Kinetics
ANN
Bio-oil

ABSTRACT

Nowadays, wearing a 3-layered face mask (3LFM) to protect against coronavirus illness (COVID-19) has become commonplace, resulting in massive, hazardous solid waste. Since most of them are infected with viruses, a secure way of disposal is necessary to prevent further virus spread. Pyrolysis treatment has recently developed as an effective method for disposing of such hazardous waste and consequently converting them into energy products. In this regard, the goal of the present study is to physicochemically characterize the 3LFM followed by pyrolysis in a TGA to evaluate the pyrolysis performance, kinetic, and thermodynamic parameters and in a semi-batch reactor to characterize the volatile product. Furthermore, an artificial neural network (ANN) was used to forecast thermal deterioration data. The results demonstrated a strong correlation between real and anticipated values. The study proved the relevance of the ANN model and the applicability of pyrolysis for disposing of 3LFM while simultaneously producing energy products.

1. Introduction

The first case of COVID-19 reported in India was on January 27 in Thrissur, Kerala. This pandemic has had a devastating impact on the community's social life, business, and health. Millions of people have been infected throughout the globe through this pandemic, with deaths of more than 2 million. In these conditions, most countries require non-pharmaceutical intercession such as wearing hand gloves, face masks, protective gown, (personal protective equipment) etc. to physically impede COVID-19 transmission. Face masks have become the first line of defence in the fight against this virus, and they have become as essential to everyday life as cell phones, clothing, and other needs. 3 Layered face mask (3LFM) are used by people abundantly due to its inexpensive cost, excellent filtering capability, very low breathing resistance, hypoallergenic characteristic, fluid resistance, and antiviral properties [1]. In spite of these benefits, 3LFM has a limited operational life of only a few days, resulting in the development of trash. As a result, disinfection and sterilisation for reuse, as well as non-certified manufacture, were offered as alternatives to disposal, reducing the quantity of waste created by 3LFM [2]. Research has shown that washing 3LFM is not preferable due to the release of microfibers, a type of pollutant [3–5]. The concerns mentioned above pose a significant barrier to mask reuse. It should be properly disposed of because many of these masks may be contaminated with the virus, as the virus can remain on the mask's surface for a longer period of time [6]. There are two categories where masks are used that require proper disposal. The first one is generated by the medical sector, such as masks used by the hospital staff, and the second one by the general public. The medical sector people disposed of the FM as medical waste while the ordinary people disposed of it as solid waste, implying catastrophic repercussions. Medical waste is often disposed of by landfill, incineration, or burning; however, these procedures have a number of drawbacks, including chronical occupation and pollution of the ocean and soil, as well as the release of harmful gases into the environment [7–9]. As a result, policy-makers must devise a secure collecting mechanism for these masks, such as establishing particular boxes in designated locations for their collection. To persuade policy-makers to do so, procedures for recycling 3LFM and converting them into supplementary energy resources must be developed [10,11].

There are different techniques (mechanical, biochemical, and thermochemical) to convert waste into useful energy forms and chemicals [12,13]. The mechanical approach is typically employed as the first step in reducing volume. The biochemical technique is preferable for transforming biological waste, in which enzymes act as a catalyst to break larger molecules into smaller ones. Combustion, pyrolysis, gasification,

* Corresponding authors.
E-mail addresses: ahmadnawaz.rs.che17@itbhu.ac.in (A. Nawaz), pkumar.che@iitbhu.ac.in (P. Kumar).

https://doi.org/10.1016/j.jtice.2022.104538
Received 22 August 2022; Received in revised form 15 September 2022; Accepted 23 September 2022
Available online 28 September 2022

and hydrothermal treatment are examples of thermochemical conversion methods. In these contexts and with this type of waste, pyrolysis is the most preferred technique to kill the virus and convert the waste into a useful energy form [14–16]. Furthermore, pyrolysis is designated as an environmentally beneficial, low-emission methodology in which medical waste may be converted into homogenous energy forms in an oxygen-free environment deprived of the need for pre-treatment in a secure environment [17–22].

Now a days ANN is widely used technique for high-accuracy modeling and prediction of systems containing nonlinear complexity. ANN are computing systems encouraged by the biological neural networks that comprise human brains. It processes components that receive input and output results depending on predetermined activation functions. ANNs are made up of several neuron layers to understand their relationship for future problem-solving tactics [23,24]. These layers include input, hidden, and output. It is demonstrated to be a valuable approach for forecasting reaction chemistry and has been used on thermal data to estimate numerous views through experimental data training, validation, and testing [25].

There is substantial literature on biomass pyrolysis, however there is a scarcity of research on thermal degradation analysis of hazardous medical waste. For example, Jung et al. valorised the COVID-19 face mask to produce bio-oil and syngas using TG-FTIR and GCMS analysis [26]. Sun et al. [27] used surgical mask for the pyrolysis process and evaluated kinetic and thermodynamic parameters. Chen et al. [28] used rope of surgical mask for the evaluation of kinetic and thermodynamic parameters based on TG-FTIR. Xu et al. [9] used thermogravimetric infrared spectroscopy and pyrolysis-gas chromatography/mass spectrometry analyses to investigate the pyrolysis mechanisms and volatiles products of medical mask belts, mask faces, and infusion tubes. Yousef et al. [29] investigated the kinetics of pyrolysis and the TG-FTIR-GC-MS analyses of coronavirus face masks. Salema et al. [30] investigated the pyrolysis and combustion kinetics of disposable surgical face mask produced during COVID-19 pandemic. Jung et al. [26] valorized the disposable COVID-19 mask through the thermochemical process. An extensive literature search revealed that a detailed systematic study of thermal degradation of 3LFM based on comprehensive pyrolysis performance index, kinetic, thermodynamic, reaction mechanism based on Criado's and Coats-Redfern method, prediction modeling using ANN (Artificial Neural Network), and thermal pyrolysis in a semi-batch reactor to produce bio-oil is still lacking. Despite the fact that these factors are crucial for the design of the reactor, performance assessment and highly accurate prediction modeling, as well as economic aspects related to potential industrial-scale upgrading.

Although there is not enough data in the literature on research related to pyrolysis of 3LFM, it can be classified as non-woven plastics waste or textile waste on the basis of their structure [31,32]. The current study sought to investigate the physicochemical properties and thermal degradation performance of 3LFM. The kinetic, thermodynamic, and reaction mechanism was evaluated based on the thermogravimetric data. Furthermore, a highly efficient artificial neural network (ANN) model was developed to forecast the thermal deterioration data. In addition, 3LFM was also thermally pyrolyzed in a semi-batch reactor. This study gives helpful information for disposing of 3LFM trash in a regulated way.

2. Materials and method

2.1. 3LFM collection and preparation

3LFM was bought from the local pharmacy store near the IIT BHU Varanasi campus. The mask used in this study was new because of the safety concerns; however, in general practice, waste 3LFM generated by both home and medical stores may be carefully separated and collected before being transferred for thermal degradation processes. The rope of the mask was taken out. The actual part of the 3LFM was then chopped and milled into small fine material using an electric grinder, resulting in lower heat transmission resistance during the pyrolysis process. It was then oven-dried overnight at 105 °C and stored in polybags to prevent moisture before being sent for further characterization.

2.2. Physicochemical characterization of 3LFM

The fundamental step before pyrolysis is a feasibility analysis of any feedstock. The proximate study such as moisture (MC), ash (AC), and volatile matter content (VM) of 3LFM was determined using the standards of ASTM such as E871, E872, and D1102, respectively, while fixed carbon (FC) content was evaluated on the difference basis (100-MC-VM-AC). The Euro-vector instrument was employed to find out the content of carbon (C), nitrogen (N), hydrogen (H), and sulphur (S). At the same time, oxygen was evaluated on the difference basis (100-C-H-N-S). An oxygen bomb calorimeter was used to calculate the calorific value. The compositional analysis such as cellulose, hemicellulose, and lignin of the 3LFM were calculated using the protocol suggested by the Technical Association of Pulp and Paper Industry (T222) [32]. All of the tests were carried out three times, with the average data being given.

2.3. FTIR spectroscopy

The FTIR spectroscopy of 3LFM was carried out to analyse the various functional groups at different peak positions using a Nicolet (Model: iS5) spectrometer. In the sample holder, 1 mg of sample was mixed with dried KBr powder in a 1:100 (percent w/w) ratio. FTIR spectra were collected between 4000 and 400 cm^{-1}.

2.4. Thermogravimetric analysis

Approximately 5 mg of 3LFM was taken in a crucible, and it was thermally analysed in a thermogravimetric analyzer (Shimadzu, Singapore, TGA 50) from room temperature to 800 °C at 10 °C/min in an inert ambient of nitrogen (100 ml/min). The pyrolysis behavior of the biomass was investigated using the same TGA apparatus at a heating rate (H.R) of 10, 20, and 40 °C/min. The investigation was conducted twice to confirm that the data was reproducible.

2.5. Pyrolysis performance study

The following equation proposed by Deng et al. [33] was used to calculate the comprehensive pyrolysis performance index (I_r):

$$I_r = \frac{\left(\frac{dw}{dt}\right)_{max}.\alpha_{\Delta T}}{T_{max}\, T_{onset} T_{endset}}$$

where I_r is the pyrolysis index, $\left(\frac{dw}{dt}\right)_{max}$ is the maximum decomposition rate, $\alpha_{\Delta T}$ is the percent weight loss in the ΔT region, T_{max} is the peak temperature, T_{onset} is the beginning devolatilization temperature, and T_{endset} is the end devolatilization temperature. Higher I_r values suggest improved pyrolysis performance.

2.6. Determination of kinetic parameters

The kinetic parameters and reaction mechanism of 3LFM were computed using the combined approaches of model-free and model fitting methods. Model-free methods such as FWO, KAS, and VZK were used to evaluate the activation energy (E) values despite knowledge of the reaction mechanism, whereas the CR technique was used to compute E values using the suggested $f(\alpha)$ and $g(\alpha)$ forms. Where $f(\alpha)$ and $g(\alpha)$ are the differential and integral conversion rate. Many processes are explored in order to find the reaction mechanism of the 3LFM, and the one that is closest to the activation energy of FWO, KAS, and VZK is the required mechanism. The following model-free equations were used to calculate the activation energy values of 3LFM pyrolysis.

2.6.1. Model-free methods

$$ln\beta = ln\frac{AE}{Rg(\alpha)} - 1.052\frac{E}{RT}\text{Ozawa} - \text{Flynn} - \text{Wall(OFW)} \quad (1)$$

$$ln\frac{\beta}{T^2} = ln\frac{AE}{Rg(\alpha)} - \frac{E}{RT}\text{Kissinger} - \text{Akahira} - \text{Sunose(KAS)} \quad (2)$$

$$\varphi = \sum_{i}^{n}\sum_{j\neq i}^{n}\frac{I(E,T_i)\beta_j}{I(E,T_j)\beta_i} = minimum\,\text{Vyazovkin method(VZK)} \quad (3)$$

Plotting the left-hand side of Eqs. (1) and (2) versus $1/T$ yields a straight line whose slope gives the activation energy (E), whereas the Senum-Yang approximation was used to estimate activation energy from VZK technique by minimising the function (φ).

2.6.2. Model fitting methods

$$ln\frac{g(\alpha)}{T^2} = ln\frac{AR}{\beta E} - \frac{E}{RT}\text{Coats Redfern method(CR)} \quad (4)$$

The value of activation energy (E) is determined by the slope of the plot between $ln\frac{g(\alpha)}{T^2}$ vs. $1/T$. The usual solid response mechanism ($g(\alpha)$) is depicted in (see supplementary material – Table S1).

2.6.3. Reaction mechanism using Criado's method

Criado's approach is used to predict reaction mechanisms by comparing theoretical and experimental plots. The $z(\alpha)$ master plot was determined using the reactions model described in the supplemental material section (Table S1). The formulae for theoretical and experimental curves are given below.

$$z(\alpha) = f(\alpha) \times g(\alpha) \quad (5)$$

$$z(\alpha) = \frac{d\alpha}{dt}exp\left(\frac{E_\alpha}{RT}\right)\int_0^T exp\left(\frac{-E_\alpha}{RT}\right) \quad (6)$$

Eq. (5) was used to generate the theoretical plot, while Eq. (6) was employed to get the actual graph. The theoretical and experimental curves were matched at particular conversion, and the ones close to the theoretical plot revealed the actual mechanism.

2.7. Thermodynamic analysis

The thermodynamic analysis was carried out by using the following equations:

$$A = \frac{\beta \times E \times e^{\frac{E}{RT_m}}}{RT_m^2} \quad (7)$$

$$\Delta H = E - RT_m \quad (8)$$

$$\Delta G = E + R \times T_m \times ln\frac{K_B \times T_m}{h \times A} \quad (9)$$

$$\Delta S = \frac{\Delta H - \Delta G}{T_m} \quad (10)$$

Where pre-exponential factor, enthalpy, Gibbs free energy, and entropy change are represented as A (s^{-1}), ΔH (kJ/mol), ΔG (kJ/mol), and ΔS (J/mol.K), respectively. The maximum peak decomposition temperature, Boltzmann constant, and Plank's constant are represented as T_m (K), K_B (1.381×10^{-23} J/K), and h (6.626×10^{-34} Js), respectively.

2.8. Artificial neural network (ANN) modeling

An ANN model was created in this work, with temperature and heating rate as input factors and weight loss (%) as output variables. The model was created using the MATLAB® 2017b toolbox, and the Levenberg-Marquardt method was employed for data prediction due to its superior performance. The 70% TGA data sets were used for training, 15% for validation, and 15% for testing. Eq. (11) was used to compute the MSE (Mean Square Error) function to assess the progress of every stage, whilst Eq. (12) was employed to optimise the network model established on the target (t) and output values (o).

$$MSE = \frac{1}{n\left[\sum_{i=1}^{n}(\lambda_i - \beta_i)^2\right]} \quad (11)$$

where λ_i and β_i are the experimental and predicted values, and n is the number of data points.

$$R^2 = 1 - \left[\frac{\sum_i (t_i - o_i)^2}{\sum_i (o_i)^2}\right] \quad (12)$$

2.9. Batch pyrolysis experiment

Thermal pyrolysis of 3LFM was performed in a laboratory-based semi-batch reactor (SS: internal diameter = 4.5 cm, height = 42 cm) in an N_2-inert atmosphere. The experimental setting is described in detail in our previous paper [34]. To fulfill the energy requirements of the operations, the system included an externally heated furnace that was governed by the PID controller. The reactor has two ports, one on top for N_2 gas and one on the bottom for volatiles release. The reactor was filled with the required feedstock and positioned vertically within the furnace. The pyrolysis experiment was performed at a heating rate of 40 °C/min, temperature of 500 °C, and N_2 flow rate of 100 ml/min. The temperature and heating rate were selected based on the thermogravimetric analysis and pyrolysis performance indices. After the experiment, the hot volatiles is condensed and collected in a bottle, while the non-condensable gases are released. After cooling the reactor to room temperature, the solid product called biochar was collected. The following formulae were then used to calculate the pyrolysis product.

$$Biochar\ yield\ (\%) = \frac{solid\ wieght}{weight\ of\ total\ sample} \times 100 \quad (13)$$

$$Bio-oil\ yield\ (\%) = \frac{liquid\ fuel\ weight}{weight\ of\ total\ sample} \times 100 \quad (14)$$

$$Gas\ yield\ (\%) = 100 - (\%liquid\ yield + \%solid\ yield) \quad (15)$$

2.10. Physicochemical characterization of 3LFM bio-oil

The physicochemical examination of pyrolytic liquid is required for its commercialization. The viscosity of the pyrolytic liquid was examined with a Brookfield viscometer at 30 °C and 50 rpm, and the bulk density was measured with a graduated cylinder and weighing machine. The oxygen bomb calorimeter was employed to assess the calorific value of the bio-oil (RS Instrument, India). A pH meter was used to determine the acidity of the bio-oil (CL-54, TI). Shimadzu QP-2010 plus apparatus with Rxi-5 ms column was utilised to conduct GCMS (gas chromatography-mass spectrometry) analysis to detect distinct compounds that existed in the bio-oil. The detailed program of the analysis is mentioned in our previous work [34,35]. The obtained mass spectra of the chemical components were compared to those in the NIST library database.

3. Results and discussion

3.1. Physicochemical characterization of 3LFM

The physicochemical characterization of 3LFM is presented in Table 1. The proximate study results revealed that 3LFM has higher volatile matter (95.4%), lower ash (4.14%), and moisture content

Table 1
Physicochemical study of 3LFM sample.

Analysis	3LFM
Proximate analysis (wt. %)	
Moisture[a]	0.31 ± 0.02
Volatile matter[b]	95.4 ± 0.38
Ash content[b]	4.14 ± .05
Fixed Carbon[b, c]	0.15
Ultimate analysis (%)	
Carbon[b]	83.68
Hydrogen[b]	14.58
Nitrogen[b]	–
Oxygen[b, c]	1.74
Sulphur[b]	–
O/C ratio	0.015
H/C ratio	2.09
Compositional analysis (wt. %)	
Hemicellulose[b]	28.65 ± 0.89
Cellulose[b]	54.21 ± 1.57
Lignin[b]	8.45 ± 0.24
Calorific value[b] (MJ/kg)	34.64 ± 0.42

(0.31%). It has previously been found that feedstock containing more volatile materials and less ash has a better ignition efficiency. Lower ash concentration raises the feedstock's heating value. It also helps to prevent fouling and slagging during boiler operations [36]. A lower moisture content (less than 10%) makes the feedstock a better choice for pyrolysis. The ultimate study results confirmed higher carbon (83.68%), and hydrogen (14.58) with negligible nitrogen and sulphur. Because of the high carbon content, face masks can be considered a viable source of carbon precursors. The negligible sulphur and nitrogen presence indicated that SOx and NOx would be almost absent during the pyrolysis process [37]. The higher heating value of the sample was found to be 34.64 MJ/kg. Further, the compositional study revealed cellulose (54.21%), hemicellulose (28.65%), and lignin (8.45%).

3.2. FTIR analysis

FTIR analysis was carried out to determine the functional groups attached to the 3LFM, as shown in Fig. 1. The characteristic peak at around 3390 cm^{-1} was due to –OH group, indicating that alcohols and water vapor were produced during the pyrolysis of the 3LFM. The absorption peaks for the C=O stretching vibration at 2365 and 2323 cm^{-1} and the absorption peak for the C=O deformation vibration at 671 cm^{-1} show that carbon dioxide was produced during the pyrolysis of the 3LFM. The absorption peaks 2950 and 2842 cm^{-1} belong to C–H stretching vibrations, whereas the absorption peaks 1425, 1363, 1315, 1222, 1029, 896, and 719 cm^{-1} correspond to C-H deformation vibrations, indicating that aliphatic compounds were formed during the pyrolysis of 3LFM. The absorption peaks 2142 and 2104 cm^{-1} for the C≡O stretching vibration suggest that carbon monoxide is produced during the pyrolysis of 3LFM. Furthermore, the absorption peaks 2733 and 2704 cm^{-1} for the C-H stretching vibration and 1717, 1681, 1646 cm^{-1} for the C=O stretching vibration show that aldehydes/ketones were produced during the pyrolysis of 3LFM.

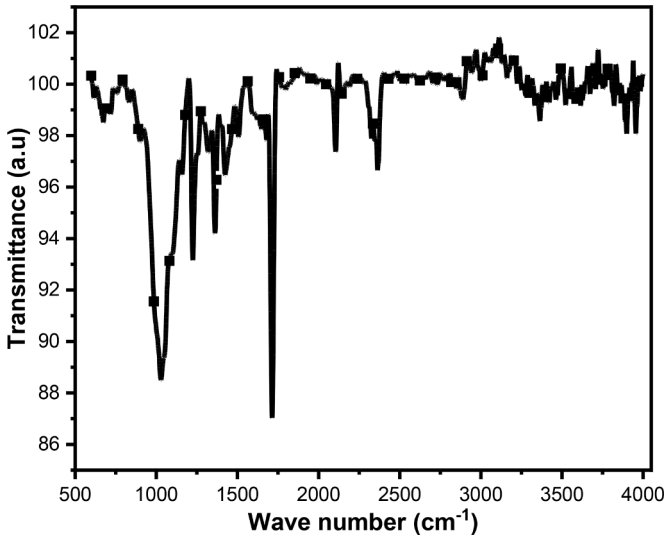

Fig. 1. FTIR spectroscopy of 3LFM sample.

3.3. Thermogravimetric analysis and effect of heating rate

Thermal analysis of the 3LFM was carried out in the temperature range of ambient to 800 °C at an H.R of 10 °C/min, as displayed in Fig. 2 (a). As seen from the TGA results (Fig. 2(a)), 3LFM underwent into three main degradation regions. These three degradation regions are drying, devolatilization, and charring. Generally, for lignocellulosic biomass, inbound surface moisture and smaller molecular-weight compounds were eliminated in the first region [38,39]. However, in the case of 3LFM during the first region (ambient to 300 °C), minor weight loss (< 0.5%) was noticed, indicating that 3LFM was thermally stable upto 300 °C and had negligible moisture content. These findings are also supported by the proximate analysis result (Table 1). The second region (300–500 °C), also known as the active pyrolysis region, represents the major degradation region. In this stage, weight loss was observed to be around 97%, owing to degradation of organic material, comprising polypropylene and melt blown filter [40,41]. The continuous flow of heat fractured larger molecular weight molecules into smaller molecular weight compounds during the second region. The third region is also known as passive pyrolysis or charring region, where almost negligible mass loss occurred. As seen from the DTG thermograph (Fig. 2(a)), generally for lignocellulosic biomass, the first peak occurred as a result of the elimination of moisture and extremely volatile chemicals that were absent in case of 3LFM DTG. Furthermore, the DTG curves (Fig. 2 (a)) revealed that only one sharp peak was noticed at 440 °C, indicating the presence of polypropylene non-woven fabrics that is generally crystalline. A similar TGA and DTG curve was also noticed by other researchers [28,42–44]. The third degradation zone, also known as the char formation region, was located above 500 °C and had no visible peak in the DTG curve, indicating total degradation of the 3LFM with negligible mass loss.

The influence of dynamic heating rates on 3LFM is depicted in Fig. 2 (b) and (c). Fig. 2 (b) and (c) showed that when heating rates increased (10 to 40 °C/min), the TG and DTG thermographs moved to higher temperature areas without altering the thermal degradation pattern. The intensity of the DTG peak increased and moved from 440 °C (at 10 °C/min) to 456 °C and 460 °C (at 20 and 40 °C/min, respectively). The shift of the TG thermograph to a higher temperature province was caused by an increase in the degradation temperature of the face mask as the heating rate increased. In comparison to a greater heating rate, heat transfer restriction was minimal at a lower heating rate. Degradation occurs slowly at higher heating rates due to heat transfer constraints, resulting in uneven heating among face masks. In contrast, a slower heating rate causes uniform heating of the face mask. Face mask interacts for a longer period of time in the reactor, resulting in maximum heat transfer among them [45].

3.4. Pyrolysis performance study

The pyrolysis performance study is presented in Table 2. As seen from the Table 2, T_{onset}, T_{endset}, and T_{max} value enhanced with enhanced heating rate. This indicates that the pyrolysis reaction has been accelerated at a higher heating rate because the reaction time for the samples to achieve the beginning devolatilization and the highest DTG peak was shortened. Maximum decomposition rate $(dw/dt)_{max}$ increased with a rise in heating rate, demonstrating that increased heating rate enhanced

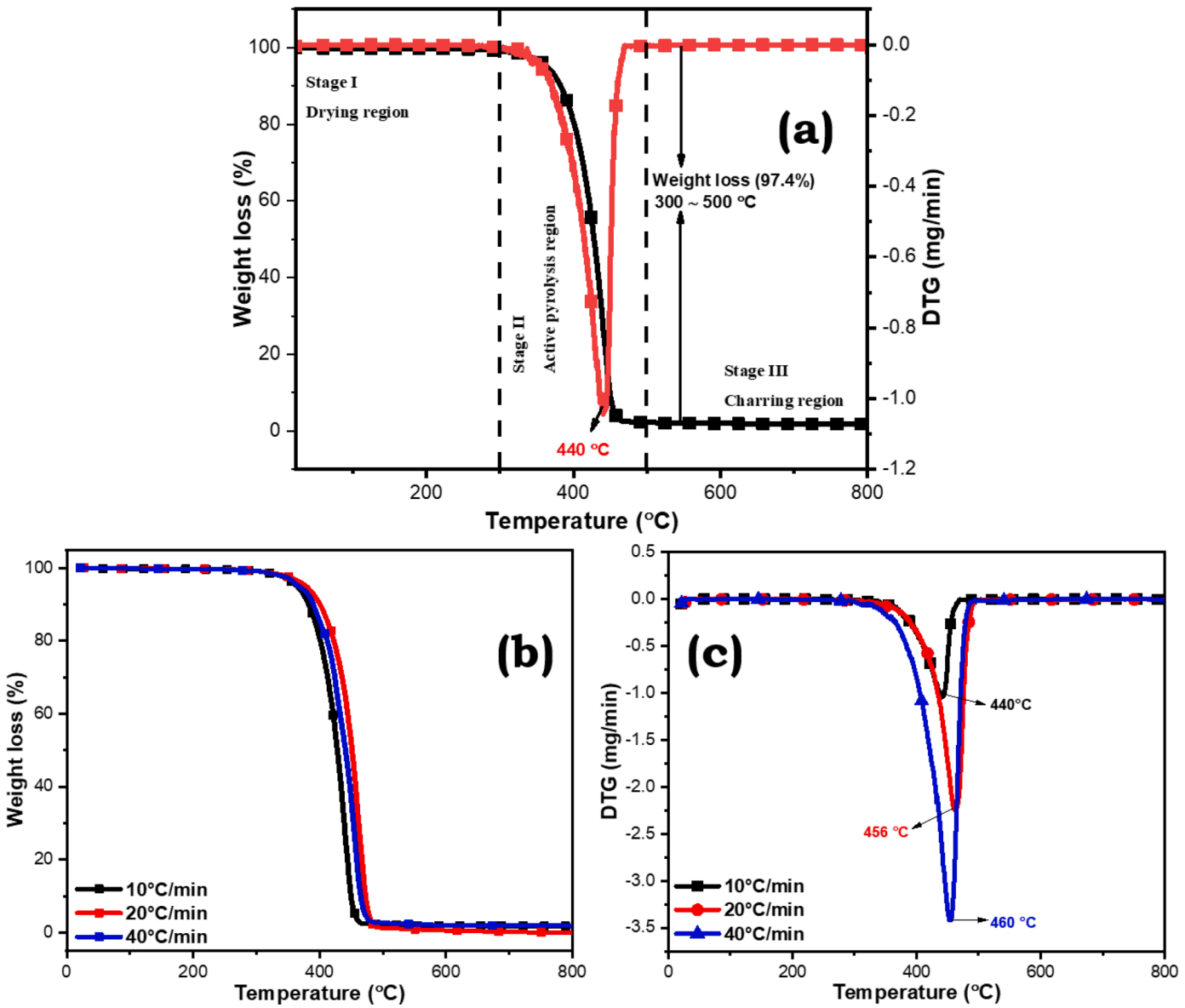

Fig. 2. (a) Thermal analysis of 3LFM at 10 °C/min, (b) TGA and (c) DTG thermograph at heating rates of 10–40 °C/min.

Table 2
Pyrolysis performance indices of 3LFM at various heating rates.

Heating rate (°C/min)	ΔT (°C)	$\alpha_{\Delta T}$ (%)	T_{onset} (°C)	T_{endset} (°C)	T_{max} (°C)	$(dw/dt)_{max}$ (mg/min)	$I_r \times 10^{-6}$
10	300–500	97.4	312	471	440.07	1.03	1.55
20	310–515	97.28	325	496	456.15	2.23	2.95
40	316–526	96.13	333	500	460.06	3.39	42.9

pyrolysis performance. The pyrolysis performance index was obtained to be 1.55, 2.95, and 42.9. This increased I_r values with heating rate implied that enhanced heating rate conditions beat lower ones since higher I_r values indicate superior performance in terms of pyrolysis efficiency. Pyrolysis performance efficiency is one of the essential operating aspects that must be addressed while designing the reactor at upto industrial level. Hence 40 °C/min is considered to be the optimum heating rate due to the highest I_r value. Further, it is reported that at a higher heating rate, bio-oil yield was high in comparison to a lower heating rate due to higher heat and mass transfer (complete pyrolysis) [46]. Pyrolysis reactions are widely known to entail both primary and secondary reactions. The secondary reaction primarily refers to the subsequent response of the first reaction products [47,48], which invariably entail radical recombination processes [49]. Because radical fragments may be created during pyrolysis from volatiles and are extremely reactive, they can combine with each other to produce additional secondary products such as coke [50]. By altering mass and heat transmission, heating rate can impact both primary and secondary processes [51].

3.5. Kinetic analysis

3.5.1. Model-free methods

The E values of 3LFM pyrolysis at specific conversion were computed using the slope of isoconversional plots as shown in Fig. 3(a) and (b) generated from the equations provided by the KAS and FWO techniques. In contrast, E values based on the VZK approach were calculated by minimizing the functionφ. The R^2 (correlation coefficient) value as given in Table 3 at each conversion level is greater than 0.97, showing its usefulness for assessing the experimental results. The activation energy values ranged from 223.77 to 241.66 kJ/mol, 223.22 to 241.33 kJ/mol,

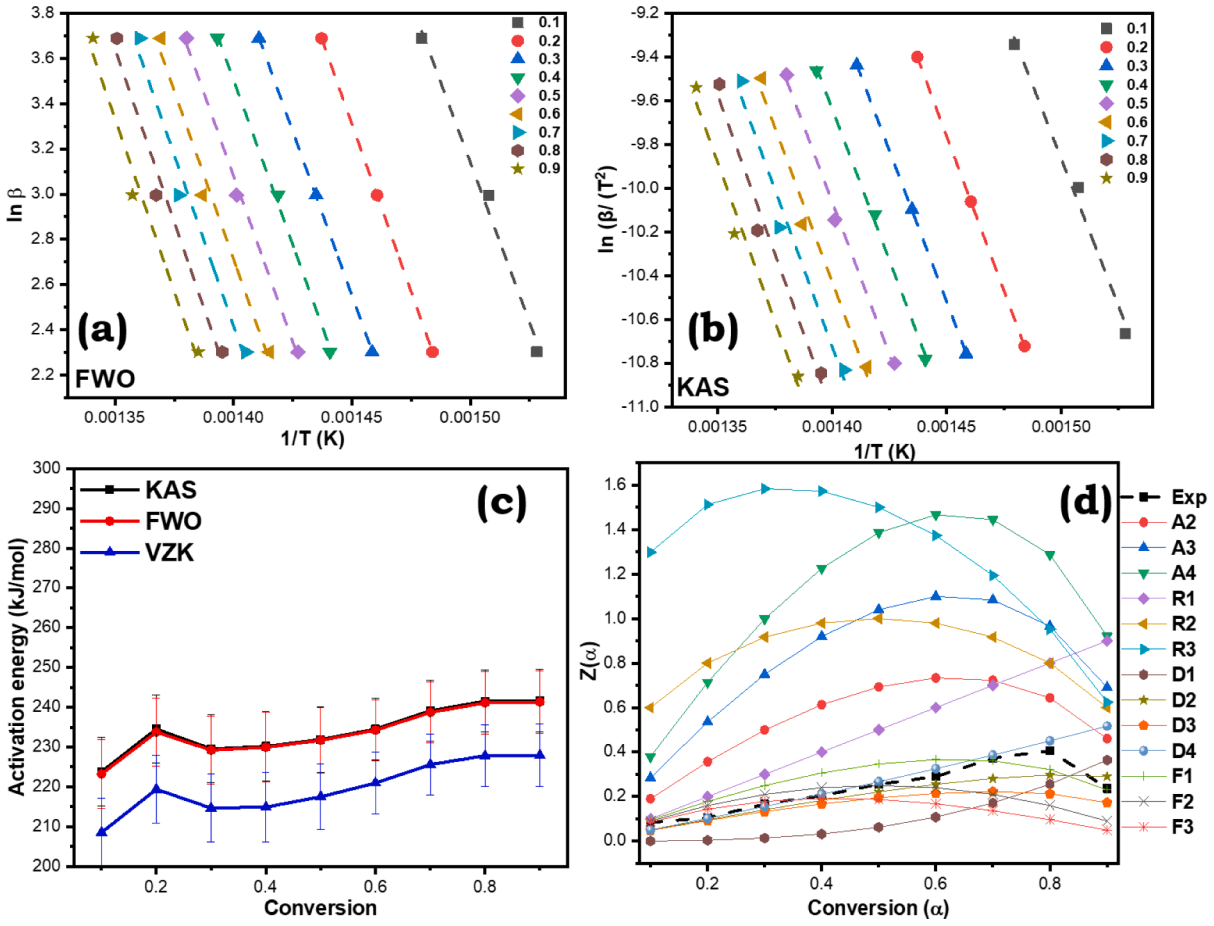

Fig. 3. (a) Isoconversional plot of FWO method, (b) KAS method, (c) alteration in *E* values with conversion, and (d) Criado *z(α)* master plot.

Table 3
Model free kinetic analysis based on KAS, FWO, and VZK method.

α	KAS E_α (kJ mol^{-1})	Equation	R^2	FWO E_α (kJ mol^{-1})	Equation	R^2	VZK E_α (kJ mol^{-1})
0.1	223.77	Y = -26916x + 30.508	0.9904	223.22	y = -28246x + 45.509	0.9913	208.53
0.2	234.52	y = -28209x + 31.14	1	233.76	y = -29579x + 46.198	1	219.38
0.3	229.54	y = -27610x + 29.514	0.9999	229.22	y = -29004x + 44.608	1	214.65
0.4	230.16	y = -27684x + 29.12	0.9978	229.94	y = -29096x + 44.239	0.9981	214.89
0.5	231.88	y = -27891x + 28.985	0.9961	231.68	y = -29316x + 44.122	0.9965	217.53
0.6	234.48	y = -28204x + 29.056	0.9804	234.24	y = -29640x + 44.209	0.9822	220.97
0.7	239.11	y = -28761x + 29.54	0.9753	238.72	y = -30207x + 44.707	0.9775	225.62
0.8	241.54	y = -29053x + 29.646	0.9772	241.11	y = -30509x + 44.826	0.9792	227.81
0.9	241.66	y = -29067x + 29.357	0.9775	241.31	y = -30534x + 44.553	0.9795	227.9
Mean	234.07			233.68			219.7

and 208.53 to 227.9 kJ/mol, with average activation energies of 234.07, 233.68, and 219.7 kJ/mol employing KAS, FWO, and VZK method, respectively. The reactivity of any fuel substantially impacts pyrolysis; it may be calculated using the activation energy [52,53]. It facilitates the optimization of numerous pyrolysis variables as well as the development of novel pyrolysis reactors. The alteration in *E* values with conversion is displayed in Fig. 3 (c). The *E* values obtained via KAS, FWO, and VZK techniques appear to have a nearly comparable style in all conversion zones. A little alteration in the *E* values estimations between models was due to the adaptation of various sorts of assumptions by the particular researcher. It can be seen from Fig. 3(c) that the lowest *E* value was found at the initial conversion (0.1). This is because, at the start of pyrolysis reaction, mostly moisture and small molecular weight compounds are present; hence lower energy is required to break this, whereas as the reaction proceeds, activation energy is increased due to requirement of more energy to break complex compounds. Further, as seen from Fig. 3(c), the activation energies value altered very little with conversion, suggesting that pyrolysis of 3LFM might be regarded as a single-step reaction. These findings are consistent with those seen in the literature for wastes of identical nature [29,32,54–56]. Furthermore, each feedstock has a distinct disintegration temperature range, and activation energy is completely temperature-dependent. Fragile bonds require less heat and energy to break down, whereas stronger bonds demand more heat and energy. Among the several models used to analyse TGA data in this work, the Vyazovkin models make no mathematical assumptions.

3.5.2. *Model fitting method*

CR method was utilised to compute the activation energies based on different reaction models at H.R of 10, 20, and 40 °C/min, as listed in

Table 4
Model fitting kinetics based on CR method.

Reaction model	10 °C/min		20 °C/min		40 °C/min		Average value
	E (kJ/mol)	R^2	*E* (kJ/mol)	R^2	*E* (kJ/mol)	R^2	*E* (kJ/mol)
A1	107.71	0.984	99.38	0.982	107.03	0.974	103.25
A2	40.73	0.656	36.03	0.622	34.8	0.525	37.18
A3	10.94	0.101	8.27	0.066	5.09	0.018	8.1
A4	3.95	0.013	5.6	0.028	9.76	0.06	6.43
R1	79.33	0.774	74.76	0.811	83.02	0.751	79.03
R2	104.2	0.904	94.88	0.899	97.67	0.878	98.91
R3	112.32	0.934	102.54	0.930	105.90	0.914	106.92
F1	130.09	0.975	119.3	0.973	123.93	0.964	124.44
F2	195.80	0.979	181.14	0.981	190.49	0.975	189.14
F3	276.98	0.915	257.52	0.919	272.72	0.908	269.07
F4	368.38	0.859	343.58	0.865	365.34	0.851	359.1
D1	214.22	0.952	196.58	0.951	206.19	0.949	205.66
D2	256.02	0.994	235.31	0.993	248.7	0.994	246.67
D3	273.27	0.993	252.32	0.993	266.14	0.991	263.91
D4	**251.14**	**0.984**	**231.44**	**0.983**	**243.69**	**0.981**	**242.09**

Table 4. The *E* values found employing model-free approaches were selected since they are not dependent on a specific kinetics process. The CR-based *E* values were used to calculate the controlling reaction mechanism. By matching the measured activation energy values of the CR method with model-free techniques, the most relevant response mechanism was established. Table 4 showed that the average activation energy derived from the reaction model D4 [$g(\alpha)$=1-(2/3)α-(1-α)$^{2/3}$] is 242.09 kJ/mol, which is comparable to that obtained from the KAS, FWO, and VZK models (229.15 kJ/mol). Therefore, three-dimensional diffusion with cylindrical symmetry is the required reaction mechanism for the pyrolysis of 3LFM. Previously, Liu et al. [57] reported that the required mechanism of pyrolysis of typical plastic waste is R2 (contracting area model), with activation energy values ranging from 140.19 to 156.12 kJ/mol in the first stage and F5 (fifth-order model) with activation energy values ranging from 231.72 to 247.75 kJ/mol in the second stage. In another investigation, Chen et al. [28] showed that the activation energy derived using the F2 model for the pyrolysis of surgical face mask rope was 260 kJ/mol, which was near to the activation energy calculated using the FWO, KAS, and VZK techniques (271 kJ/mol). The current study is consistent with the previously published literature.

3.6. *Z(α) master plot*

Pyrolysis of any feedstock is a complex process that comprises a variety of series and parallel reactions occurring at the same time. As a result, establishing the response mechanism of such a complex process is highly difficult. A mechanistic model based on appropriate mathematical approximation has been presented to predict the response mechanism of such complex systems. The Criado's $z(\alpha)$ master plot was employed to deduce the reaction mechanism of such a complex process. Eqs. (5) and (6) were used to get the theoretical and experimental curves. The functions $f(\alpha)$ and $g(\alpha)$ can be obtained from the supplementary section (Table S1). Four different forms of regulatory mechanisms, such as An, Rn, Dn, and Fn, were used to identify the response mechanism. Where An is the nucleation and growth control, Rn is the phase boundary control, Dn is the diffusion control, and Fn is the random nucleation control. As seen in Fig. 3(d), the experimental curve overlapped D4 theoretical curve in between conversion 0.1–0.8, which is associated with the diffusion mechanism on 3-D; however, in conversion 0.8–0.9, the experimental curve only crosses D1 and D2 theoretical curve. As a result, no precise response mechanism can be inferred between the conversions of 0.8–0.9. The current finding revealed that pyrolysis of 3LFM followed a single reaction mechanism over the conversion range of 0.1–0.8. This finding is consistent with the fluctuation of *E* values with regard to α (Fig. 3(c)), where there is a very little alteration in *E* values with respect to α. Interestingly, it is also well matched with the reaction mechanism obtained from the CR method. However, it is well known that both methods have different approximations and assumptions.

3.7. *Thermodynamic analysis*

Thermodynamic analysis was carried out at each H.R (10, 20, and 40 °C/min) using the activation energy from VZK method, as presented in Table 5. The average *A* value was 5.0105E + 15, 2.1587E + 15, and 1.86333E + 15 s^{-1} at H.R of 10, 20, and 40 °C/min, respectively. More precisely it altered from 4.37692E + 14–1.25452E + 16, 2.00328E + 14–5.34464E + 15, and 1.75471E + 14–4.60057E + 15 s^{-1} in the conversion range 0.1–0.9 at H.R of 10, 20, and 40 °C/min, respectively. This high pre-exponential factor value (>10^9 s^{-1}) indicates that there was no surface reaction and that chemical complexes were synthesised prior to the formation of end products in the 3LFM pyrolysis. The average value of change in enthalpy (ΔH) is obtained to be 213.91, 213.8, and 213.71 kJ/mol at H.R of 10, 20, and 40 °C/min, respectively. More precisely, it altered from 203.09–221.9, 203.02–221.77, and 202.91–221.7 kJ/mol at H.R of 10, 20, and 40 °C/min, respectively. It is earlier reported that during a single reaction, a change in enthalpy represents the difference in energy between reactants and products [58]. Furthermore, as shown in Fig. 4(a), the ΔH value is positive for each conversion, indicating that the energy of the reactant is less than the energy of the product. Thermal degradation is most likely if the difference between the average ΔH and *E* values does not exceed 7 kJ/mol [59]. Tables 3 and 5 showed that the difference between ΔH and *E* values at each conversion level does not exceed 6.2 kJ/mol. This illustrates that the potential energy barrier is easily overcome during 3LFM pyrolysis, and the product produced is viable. ΔG, as displayed in Fig. 4(b), represents the possibility and difficulty of a specific reaction happening. The greater the ΔG value, less likely the associated response. Furthermore, if ΔG is positive, the related response may not happen on its own. At H.R of 10, 20, and 40 °C/min, the average value of ΔG is 188.17, 192.58, and 193.34 kJ/mol, respectively. The presence of positive values of ΔG at respective H.R and individual conversion implies that pyrolysis of the 3LFM is a nonspontaneous process that occurs only when external energy is supplied. Change in entropy (ΔS) represents the degree of unpredictability in the system. The average value of change in enthalpy (ΔS) is obtained to be 36.09, 29.1, and 27.8 J/mol.K at H.R of 10, 20, and 40 °C/min, respectively. More precisely it altered from 20.49–47.6, 13.88–40.38, and 12.63–38.99 kJ/mol at H.R of 10, 20, and 40 °C/min, respectively. If the ΔS value is negative, it means that the related reaction system's disorder degree reduces after the reaction occurs, and the disorder degree of the reactants is greater than that of the products. It can be seen from the Fig. 4(c) that at all the conversion, ΔS value is positive. It means products formed by bond dissociations had a

Table 5
Thermodynamic analysis of pyrolysis of 3LFM.

β (°C/min)	Conversion	A(1/sec)	ΔH(kJ/mol)	ΔG(kJ/mol)	ΔS(J/mol.K)
10°C/min	0.1	4.37692E + 14	203.09	188.47	20.49
	0.2	2.87065E + 15	213.78	188.17	35.9
	0.3	1.2637E + 15	208.94	188.3	28.94
	0.4	1.31797E + 15	209.12	188.3	29.2
	0.5	2.08188E + 15	211.7	188.22	32.92
	0.6	3.78231E + 15	215.1	188.13	37.82
	0.7	8.45081E + 15	219.7	188.01	44.44
	0.8	1.23443E + 16	221.85	187.95	47.53
	0.9	1.25452E + 16	221.9	187.95	47.6
	Average	5.0105E + 15	213.91	188.17	36.09
20°C/min	0.1	2.00328E + 14	203.02	192.9	13.88
	0.2	1.26215E + 15	213.69	192.59	28.94
	0.3	5.65441E + 14	208.85	192.72	22.12
	0.4	5.89196E + 14	209.03	192.71	22.37
	0.5	9.21658E + 14	211.59	192.64	25.99
	0.6	1.65322E + 15	214.98	192.55	30.77
	0.7	3.63085E + 15	219.58	192.42	37.25
	0.8	5.26085E + 15	221.73	192.36	40.27
	0.9	5.34464E + 15	221.77	192.36	40.34
	Average	2.1587E + 15	213.8	192.58	29.1
40°C/min	0.1	1.75471E + 14	202.91	193.65	12.63
	0.2	1.0948E + 15	213.6	193.34	27.62
	0.3	4.92562E + 14	208.75	193.48	20.84
	0.4	5.13144E + 14	208.92	193.47	21.08
	0.5	8.00788E + 14	211.5	193.39	24.7
	0.6	1.43196E + 15	214.9	193.3	29.47
	0.7	3.1318E + 15	219.5	193.17	35.92
	0.8	4.52883E + 15	221.65	193.11	38.92
	0.9	4.60057E + 15	221.7	193.11	38.99
	Average	1.86333E + 15	213.71	193.34	27.8

higher degree of disorderness than the reactants. Further, as seen from Fig. 4, H.R has very little effect on thermodynamic parameters. Change in enthalpy decreases marginally at particular conversion. At the same conversion and with increase in H.R from 10 to 20 °C/min, ΔG value increases by approximately 4 kJ/mol. Interestingly, on increasing H.R from 20 to 40 °C/min, it increases only by 1 kJ/mol. This is because as H.R raised, the motion of the reactant molecules increased causing thermal degradation of 3LFM simpler. The ΔS value with rise in H.R is still positive, however it decreased with rise in H.R. The decrease in ΔS value with rise in H.R decreases the degree of randomness during bond dissociation.

3.8. Kinetic compensation effect

The kinetic compensation effect is used to characterise the relationship between activation energy and logarithmic pre-exponential factor. The kinetic compensation effect is governed by the equation: $ln\ A = a + bE$. In this equation, a and b are defined as $a = ln\ k_{iso}$, and $b = 1/(RT_{iso})$, where T_{iso} and k_{iso} are the isokinetic temperature and rate, respectively. Suppose the T_{iso} values at different heating rates are within the active pyrolysis temperature range. In that case, the calculated kinetic parameters are acceptable. Fig. 4(d) showed the change in activation energy, the logarithmic pre-exponential factor, and values for the compensating parameters (d). T_{iso} values of 694.41, 709.56, and 713.35 K at H.R of 10, 20, and 40 °C/min are all well within the active pyrolysis temperature range of 573.15 to 799.15 K. Further, the regression coefficient (R^2) value is equal to 1, which validated the accuracy of the calculated kinetic parameters.

3.9. Artificial neural network modelling

The findings of the TGA analysis were utilised to build an extremely efficient ANN model. Based on experimental data sets, this ANN model was created to anticipate pyrolysis data using a feed-forward back propagation technique. When predicting the accuracy and performance of the ANN model, the number of neurons in the input and output layers is fixed; the number of neurons in the hidden layer is the variable that may be controlled. Initially, a hidden layer is developed in order to have a simpler ANN model. The most efficient structure was identified to be 2*10*1, which was chosen based on the R^2 value and MSE (mean square error) as the second criteria. The model was created by arbitrarily partitioning the entire 8207 datasets into 5745 for training (70%). Another set of 1231 trials was used to validate (15%) and evaluate (15%) the established model. The validation and testing steps are crucial for verifying the correctness of the created model and its future applicability in forecasting output under changing process conditions. Fig. 5 depicts four separate graphs: training, regression, performance, and error histogram. The training state graph (Fig. 5(a)) illustrates the alteration in the amplitude of the gradient and the number of validation checks with an increase in iterations (or epochs). A total of 241 iterations were carried out in the inquiry, according to the performance graph in Fig. 5 (b), with iteration 235 showing the best validation achievement with an MSE of 0.00022291 and R^2 value of 0.99. In all training, validation, and testing phases, regression graphs (Fig. 5(c)) revealed high R^2 value, demonstrating how accurate and effective the constructed ANN model is in forecasting the outcomes of pyrolysis. Furthermore, along with a high R^2 value, the model's appropriateness is demonstrated by a low MSE value (Fig. 5(c)). The neural network's accuracy is demonstrated by the error histogram plot (Fig. 5(d)), which compares the anticipated and empirically determined target values. The majority of the inaccuracies, as shown in Fig. 5(d), are within a ± 1 range, which is acceptable. The network performance was validated using regression and histogram graphs. The resulting model's strong ability to predict the outcomes of pyrolysis is demonstrated by its high overall R^2 value of 0.99.

3.9.1. Validation of the feasibility of ANN model

The mass loss data (mg) obtained via ANN was used to predict the α and dα/dT at H.R of 10, 20, and 40 °C/min. The experimentally determined and ANN-based mass loss data are plotted in Fig. 6. It showed that both data are very close to each other, with a strong correlation coefficient (R^2 = 0.999) at each heating rate. Further, the comparison between the experimentally determined and ANN-predicted α and $d\alpha/dT$ values with respect to temperature at each heating rate in the active pyrolysis zone is depicted in Fig. 7. The experimentally determined and ANN predicted values almost perfectly overlap each other, as shown in the relevant Fig. 7. The slight variations between the actual and ANN predicted values might be due to errors arising because of the inexact TG result at high and low α [60].

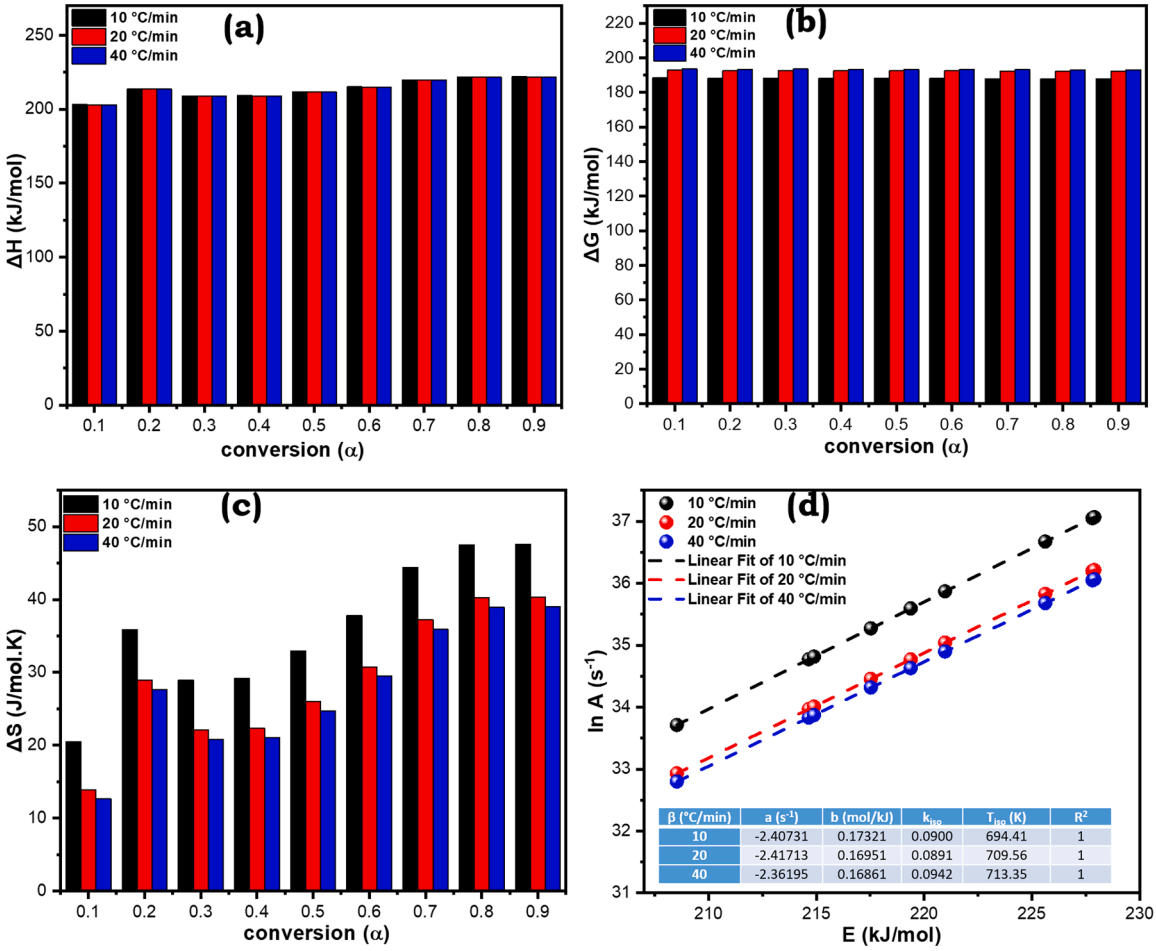

Fig. 4. (a) Change in ΔH, (b) Change in ΔG, (c) Change in ΔS with respect to conversion, and (d) kinetic compensation effect at all heating rates.

3.10. Physicochemical characterization of bio-oil

The physicochemical properties (Table 6) of bio-oil produced after pyrolysis of 3LFM at 500 °C and a heating rate of 40 °C/min were investigated. The yield of the bio-oil at this condition was 46.72%. The colour of the bio-oil was seen to be black, and its odour was smoky. The pH of the bio-oil was 4.83. This is the major disadvantage of bio-oil might be due to the attendance of different types of organic acids. The low pH causes decreased HHV and induce corrosion in boilers and pipelines during its application [61]. Hence up-gradation of bio-oil, such as catalytic cracking, is necessary to enhance the pH value. The viscosity of the bio-oil was 4.75 cSt, comparable to diesel fuel. Viscosity plays an essential role design and injection of fuel. In general, bio-oil supplemented with increased viscosity has a negative influence on flame temperature and fluidity, which may cause engine damage during combustion [62]. The density of bio-oil is 860 kg/m^3, greater than gasoline and diesel fuel. The high density was due to the presence of complex organic molecules in the bio-oil. The HHV of the liquid fuel was 24.54 MJ/kg, significantly less than the diesel and gasoline fuel. This may be because there are more organic acids present. Finally, it was discovered that the ash concentration was 0.22 and that there was 3.25 weight percent of ramsbottom carbon residue, which indicates that bio-oil has a tendency to produce carbon at high temperatures.

3.11. GCMS of 3LFM bio-oil

Gas chromatography-mass spectroscopy of the bio-oil was carried out, and the obtained mass spectra were matched with the NIST (National Institute of Standards and Technology) library database to recognise the unknown compounds. It should be noted that only compounds having an area percentage greater than one are considered in this study. The details of the identified compounds are presented in the supplementary material section (Table S2 and Fig. S1). It is evident that bio-oil obtained through pyrolysis of lignocellulosic biomass typically contained hydrocarbons, acids, esters, ethers, aldehydes, benzene derivatives, oxygenated compounds, phenols etc., in sufficient quantity [35]; however, the bio-oil obtained after pyrolysis of polymeric material (non-woven fabrics) mostly contained hydrocarbons. The presence of these compounds causes bio-oil to be effective in industrial applications. The composition of bio-oil significantly changes with changes in feedstock, reactor, type of pyrolysis, operating condition, etc. In this study, based on GCMS analysis, the hydrocarbon, acids, ether, ester, ketone alcohol, bromine-containing, phenol, benzene derivatives, and oxygen-containing compounds account for 79.58, 6.53, 0.88, 1.3, 2.73, 1.03, 1.05, 1.09, 4.35, 0.28, and 1.18%, respectively. The major compounds identified in the bio-oil are: hexadecane (13.01%), nonadecane (10.09%), pentadecane (6.54%), heptadecane (4.87%), tridecane (3.61%), pentadecane, 2, 6, 10-trimethyl (3.46%), phytane (2.69%), 1, 2-Benzenedicarboxylic acid (2.55%), 1, 2-Benzenedicarboxylic acid, dioctyl ester (2.42%). Further, Yousef et al. [63] pyrolyzed waste surgical mask in a pyrolysis reactor at 25°C/min heating rate and at four different temperatures. The GCMS results revealed that the major compounds identified in all of the pyrolyzed samples were 2,4-Dimethyl-1-heptene (12.5-23.8%), 2-Undecene, 4-methyl- (4.7–7.3%), 2-Acetylcyclopentanone (4.75–14.5%), and 4-Isopropyl-1, 3-cyclohexanedione (9–11.7%). In an another study conducted by Yousef et al. [56], 3PFM was thermally and catalytically pyrolyzed using ZSM-5 in a TG-MS. The results revealed that 1-butanol (19.7–31.2%)

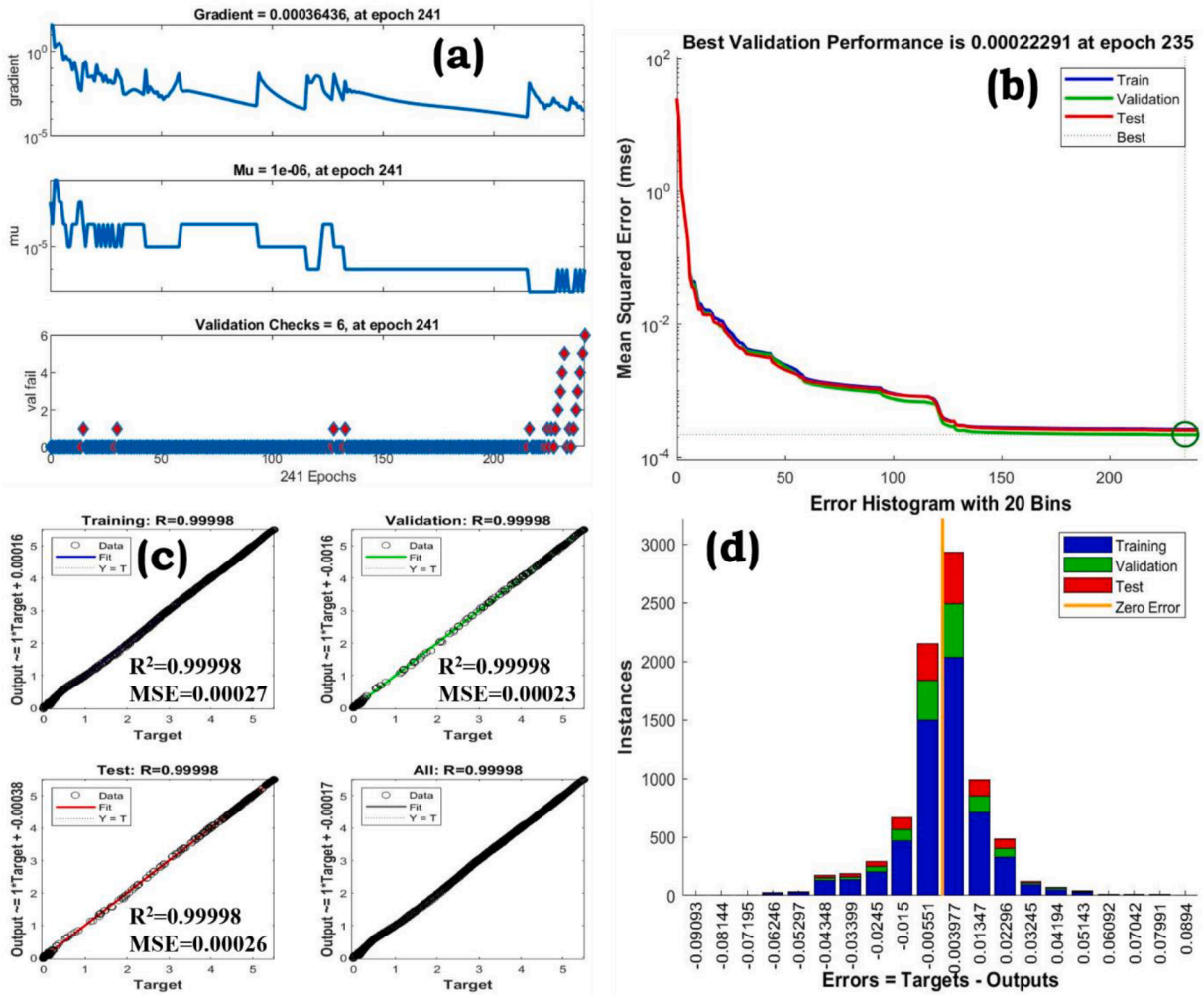

Fig. 5. (a) Training, (b) performance, (c) regression analysis, and (d) error histogram.

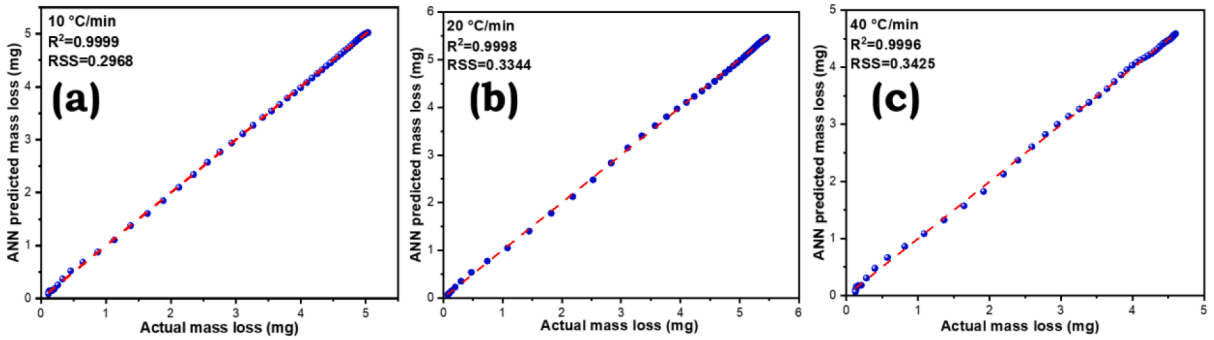

Fig. 6. Experimentally determined and ANN predicted mass loss data (a) 10, (b) 20, and (c) 40 °C/min.

and carbon dioxide (41.6–63.6%) were the two primary components in the volatile products produced at the 5 °C/min, whereas at 30 °C/min, the same chemicals were produced in greater quantity, especially carbon dioxide (55.9–69.5%) and 1-butanol (12–30.4%). Additionally, pentane, 2,4-Dimethyl-1-heptene, 2-Acetylcyclopentanone, and other significant compounds were detected when Yousef et al. [29] pyrolyzed a 3-ply face mask using a TG-MS. In the present study the presence of oxygen-containing molecules such as acids, alcohol, ester, and ketone is reduced, increasing the stability of a separated liquid. Acids inherent in bio-oil cause corrosion of metals, making transportation, consumption, and preservation of bio-oil a serious difficulty that must be addressed prior to commercialisation. The higher percentage of hydrocarbons in the bio-oil was due to commencement of decarboxylation processes, which enhanced hydrocarbon production [64]. The significantly higher hydrocarbon percentage could replace conventional fuel; however, the presence of acids in the bio-oil prevents this. Hence bio-oil should be modified before commercialization as a conventional fuel; however, it can be used for house cooking or extraction of useful chemicals.

3.12. Pyrolysis reaction pathways

Using the three monomers as an example displayed in Fig. 8, the

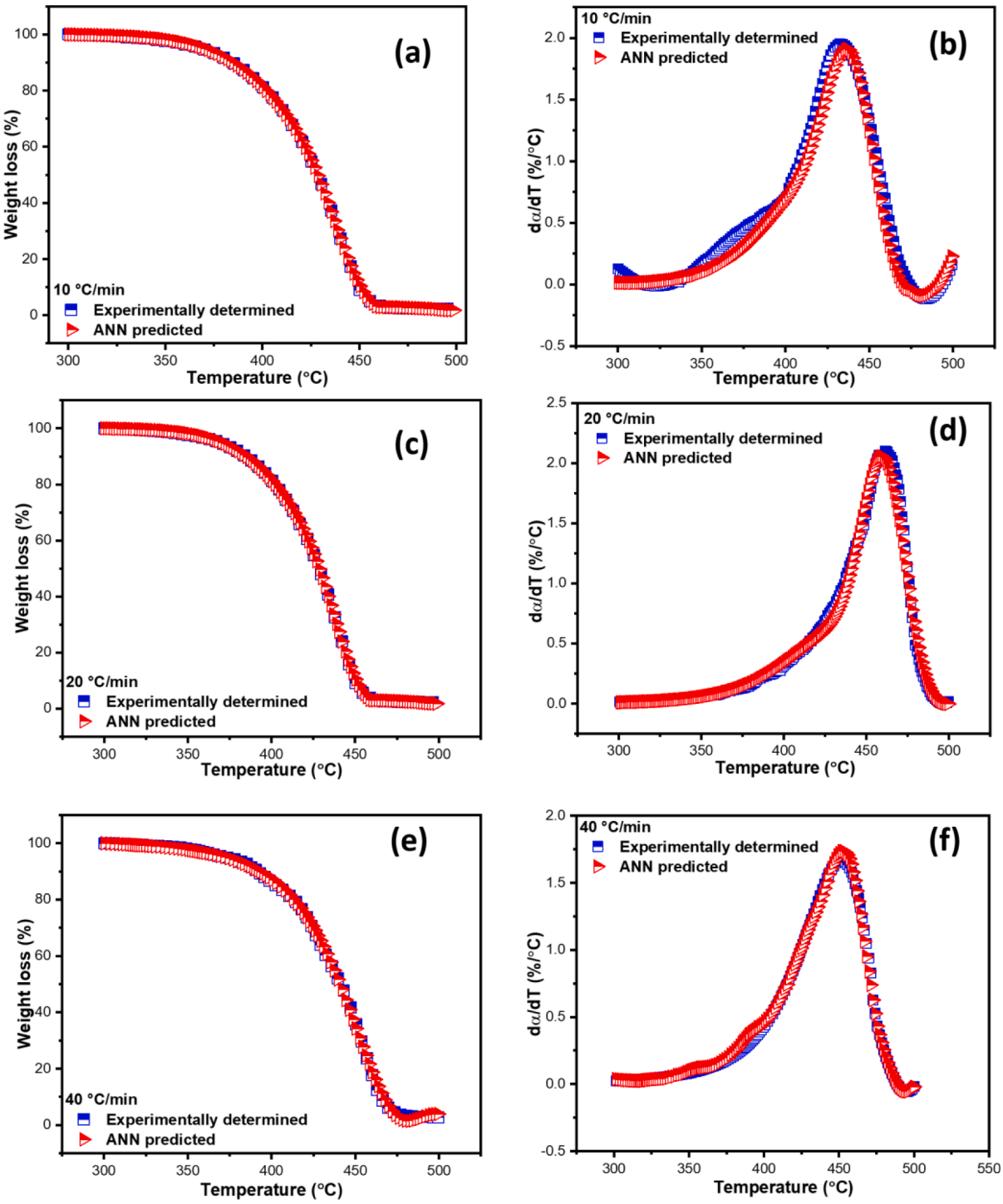

Fig. 7. TGA and DTG of experimental and ANN predicted data in the active pyrolysis zone.

Table 6
Physicochemical properties of 3LFM bio-oil compared to diesel and gasoline.

Analysis	LS bio-oil	Diesel	Gasoline
Odour	Smoky	–	–
Colour	Black	–	–
Acidity	4.83 ± 0.18	–	–
Viscosity (cSt) (30°C) (50 rpm)	4.75 ± 0.25	2–4	0.12
Density(kg/m^3)	860 ± 3.84	828	838
HHV (MJ/kg)	24.54 ± 0.34	44.5	47.3
Ash Content (wt. %)	0.22 ± 0.08	–	–
Ramsbottom carbon residue (wt. %)	3.25 ± 0.05	–	–

process of intramolecular hydrogen transfer following random breaking was used to explain the pyrolysis of polypropylene in 3LFM [9]. Intermolecular hydrogen transfer, β-fracture, and intermolecular hydrogen extraction processes were all part of the pyrolysis process [65]. The fracture position can be A or B, resulting in the formation of the four chain structures a, b, c, and d, respectively, and then continuing to break to generate dienes, alkanes, and cycloalkanes. Short-chain hydrocarbons and long-chain hydrocarbons were also produced during the process.

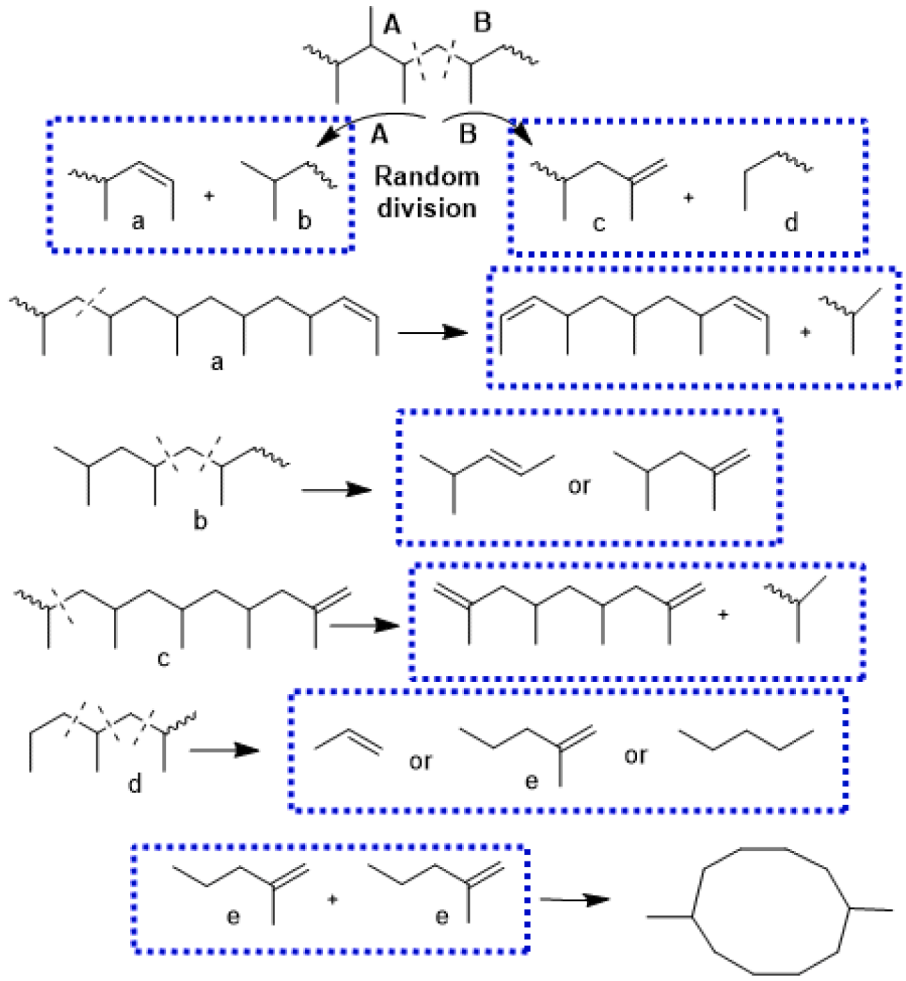

Fig. 8. Pyrolysis reation pathway of 3LFM sample.

4. Conclusion

3LFM had been successfully pyrolyzed in a TGA and semi-batch reactor to evaluate its pyrolysis performance and bioenergy potential. The physicochemical analysis results revealed higher volatile matter (95.4%) and negligible moisture content (0.31%). The pyrolysis performance indices revealed improved pyrolysis efficiency at the highest heating rate (40 °C/min) and is most appropriate for the thermal degradation process to achieve the desired product. The kinetic analysis results revealed average values gained from KAS, FWO, and VZK methods are 234.07, 233.68, and 219.7 kJ/mol, respectively. The CR and master plot method revealed that three-dimensional diffusion with cylindrical symmetry D4 [$g(\alpha)$=1-(2/3)α-(1-α)$^{2/3}$] is the required reaction mechanism of the pyrolysis of 3LFM. The kinetic compensation effect revealed that the values of T_{iso} at each heating are well within the active pyrolysis temperature range. The potential energy barrier is easily crossed, and the product generated is viable, as indicated by thermodynamic analysis. The experimentally determined and ANN predicted values almost perfectly overlap each other, indicating that ANN corresponded well with the thermogravimetric data, and it might be used in pyrolysis to better understand such a complicated process. The GCMS analysis revealed higher hydrocarbons and lower oxygenated compounds. These findings imply that pyrolysis treatment might be used to decompose hazardous 3LFM, which has a large potential for use in the renewable energy industry, resulting in fewer environmental problems.

Declaration of Competing Interest

The authors declare that they have no known competing financial interests or personal relationships that could have appeared to influence the work reported in this paper.

Acknowledgment

The authors would like to acknowledge Department of Chemical Engineering & Technology and Central Instrument Facility Centre of IIT BHU Varanasi for providing the necessary facilities to carry out this research.

Supplementary materials

Supplementary material associated with this article can be found, in the online version, at doi:10.1016/j.jtice.2022.104538.

References

[1] Scerri M, Grech V. To wear or not to wear? Adherence to face mask use during the COVID-19 and Spanish influenza pandemics. Early Hum Dev 2020:105253. https://doi.org/10.1016/j.earlhumdev.2020.105253.
[2] Wang J, Pan L, Tang S, Ji JS, Shi X. Mask use during COVID-19: a risk adjusted strategy. Environ Pollut 2020;266:115099. https://doi.org/10.1016/j.envpol.2020.115099.
[3] Rubio-Romero JC, Pardo-Ferreira MDC, Torrecilla-García JA, Calero-Castro S. Disposable masks: disinfection and sterilization for reuse, and non-certified manufacturing, in the face of shortages during the COVID-19 pandemic. Saf Sci 2020;129:104830. https://doi.org/10.1016/j.ssci.2020.104830.

[4] Fadare OO, Okoffo ED. COVID-19 face masks: a potential source of microplastic fibers in the environment. Sci Total Environ 2020;737:140279. https://doi.org/10.1016/j.scitotenv.2020.140279.

[5] Aragaw TA. Surgical face masks as a potential source for microplastic pollution in the COVID-19 scenario. Mar Pollut Bull 2020;159:111517. https://doi.org/10.1016/j.marpolbul.2020.111517.

[6] Shruti VC, Pérez-Guevara F, Elizalde-Martínez I, Kutralam-Muniasamy G. Reusable masks for COVID-19: a missing piece of the microplastic problem during the global health crisis. Mar Pollut Bull 2020;161:111777. https://doi.org/10.1016/j.marpolbul.2020.111777.

[7] Rowan NJ, Laffey JG. Unlocking the surge in demand for personal and protective equipment (PPE) and improvised face coverings arising from coronavirus disease (COVID-19) pandemic - implications for efficacy, re-use and sustainable waste management. Sci Total Environ 2021;752:142259. https://doi.org/10.1016/j.scitotenv.2020.142259.

[8] Sangkham S. Face mask and medical waste disposal during the novel COVID-19 pandemic in Asia. Case Stud Chem Environ Eng 2020;2:100052. https://doi.org/10.1016/j.cscee.2020.100052.

[9] Xu W, Liu J, Ding Z, Fu J, Evrendilek F, Xie W, et al. Dynamic pyrolytic reaction mechanisms, pathways, and products of medical masks and infusion tubes. Sci Total Environ 2022;842:156710. https://doi.org/10.1016/J.SCITOTENV.2022.156710.

[10] Nowakowski P, Kuśnierz S, Sosna P, Mauer J, Maj D. Disposal of personal protective equipment during the COVID-19 pandemic is a challenge for waste collection companies and society: a case study in Poland. Resources 2020;9. https://doi.org/10.3390/resources9100116.

[11] Tang X, Chen X, He Y, Evrendilek F, Chen Z, Liu J. Co-pyrolytic performances, mechanisms, gases, oils, and chars of textile dyeing sludge and waste shared bike tires under varying conditions. Chem Eng J 2022;428:131053. https://doi.org/10.1016/J.CEJ.2021.131053.

[12] Halim SA, Mohd NA, Razali NA. A comparative assessment of biofuel products from rice husk and oil palm empty fruit bunch obtained from conventional and microwave pyrolysis. J Taiwan Inst Chem Eng 2022;134:104305. https://doi.org/10.1016/J.JTICE.2022.104305.

[13] Sewu DD, Lee DS, Tran HN, Woo SH. Effect of bentonite-mineral co-pyrolysis with macroalgae on physicochemical property and dye uptake capacity of bentonite/biochar composite. J Taiwan Inst Chem Eng 2019;104:106–13. https://doi.org/10.1016/J.JTICE.2019.08.017.

[14] Tripathi A, Tyagi VK, Vivekanand V, Bose P, Suthar S. Challenges, opportunities and progress in solid waste management during COVID-19 pandemic. Case Stud Chem Environ Eng 2020;2:100060. https://doi.org/10.1016/j.cscee.2020.100060.

[15] Yousef S, Kuliešienė N, Sakalauskaitė S, Nenartavičius T, Daugelavičius R. Sustainable green strategy for recovery of glucose from end-of-life euro banknotes. Waste Manag 2021;123:23–32. https://doi.org/10.1016/j.wasman.2021.01.007.

[16] Sharma HB, Vanapalli KR, Cheela VRS, Ranjan VP, Jaglan AK, Dubey B, et al. Challenges, opportunities, and innovations for effective solid waste management during and post COVID-19 pandemic. Resour Conserv Recycl 2020;162:105052. https://doi.org/10.1016/j.resconrec.2020.105052.

[17] Filimonau V. The prospects of waste management in the hospitality sector post COVID-19. Resour Conserv Recycl 2021;168:105272. https://doi.org/10.1016/j.resconrec.2020.105272.

[18] Fu J, Liu J, Xu W, Chen Z, Evrendilek F, Sun S. Torrefaction, temperature, and heating rate dependencies of pyrolysis of coffee grounds: its performances, bio-oils, and emissions. Bioresour Technol 2022;345:126346. https://doi.org/10.1016/J.BIORTECH.2021.126346.

[19] Hernowo P, Steven S, Restiawaty E, Bindar Y. Nature of mathematical model in lignocellulosic biomass pyrolysis process kinetic using volatile state approach. J Taiwan Inst Chem Eng 2022;139:104520. https://doi.org/10.1016/J.JTICE.2022.104520.

[20] Khavari Farid R, Rahimi G. Oilothermal, a novel pyrolysis method for fabrication of carbon dots-loaded carriers from cyanobacteria for use in solid-phase extraction of cadmium. J Taiwan Inst Chem Eng 2022;132:104210. https://doi.org/10.1016/J.JTICE.2022.104210.

[21] Xu J, Brodu N, Devougue-Boyer C, Youssef B, Taouk B. Biobased novolac resins cured with DGEBA using water-insoluble fraction of pyrolysis bio-oil: synthesis and characterization. J Taiwan Inst Chem Eng 2022;138:104464. https://doi.org/10.1016/J.JTICE.2022.104464.

[22] Pandey VK, Verma S, Verma B. Polyaniline/activated carbon/copper ferrite (PANI/AC/CuF) based ternary composite as an efficient electrode material for supercapacitor. Chem Phys Lett 2022;802:139780. https://doi.org/10.1016/J.CPLETT.2022.139780.

[23] Ahmad MS, Mehmood MA, Taqvi STH, Elkamel A, Liu CG, Xu J, et al. Pyrolysis, kinetics analysis, thermodynamics parameters and reaction mechanism of Typha latifolia to evaluate its bioenergy potential. Bioresour Technol 2017;245:491–501. https://doi.org/10.1016/j.biortech.2017.08.162.

[24] Ding Z, Chen Z, Liu J, Evrendilek F, He Y, Xie W. Co-combustion, life-cycle circularity, and artificial intelligence-based multi-objective optimization of two plastics and textile dyeing sludge. J Hazard Mater 2022;426:128069. https://doi.org/10.1016/J.JHAZMAT.2021.128069.

[25] Chen J, Liu J, He Y, Huang L, Sun S, Sun J, et al. Investigation of co-combustion characteristics of sewage sludge and coffee grounds mixtures using thermogravimetric analysis coupled to artificial neural networks modeling. Bioresour Technol 2017;225:234–45. https://doi.org/10.1016/J.BIORTECH.2016.11.069.

[26] Jung S, Lee S, Dou X, Kwon EE. Valorization of disposable COVID-19 mask through the thermo-chemical process. Chem Eng J 2021;405:126658. https://doi.org/10.1016/j.cej.2020.126658.

[27] Sun S, Yuan Y, Chen R, Xu X, Zhang D. Kinetic, thermodynamic and chemical reaction analyses of typical surgical face mask waste pyrolysis. Therm Sci Eng Prog 2021;26:101135. https://doi.org/10.1016/j.tsep.2021.101135.

[28] Chen R, Zhang D, Xu X, Yuan Y. Pyrolysis characteristics, kinetics, thermodynamics and volatile products of waste medical surgical mask rope by thermogravimetry and online thermogravimetry-Fourier transform infrared-mass spectrometry analysis. Fuel 2021;295:120632. https://doi.org/10.1016/j.fuel.2021.120632.

[29] Yousef S, Eimontas J, Striūgas N, Abdelnaby MA. Pyrolysis kinetic behaviour and TG-FTIR-GC–MS analysis of coronavirus face masks. J Anal Appl Pyrolysis 2021;156:105118. https://doi.org/10.1016/J.JAAP.2021.105118.

[30] Salema AA, Mohd Zaifullizan Y, Wong WH. Pyrolysis and combustion kinetics of disposable surgical face mask produced during COVID-19 pandemic. Energy Sources A Recovery Util Environ Eff 2022;44:566–76. https://doi.org/10.1080/15567036.2022.2048140.

[31] Yousef S, Tatariants M, Tichonovas M, Kliucininkas L, Lukošiūtė SI, Yan L. Sustainable green technology for recovery of cotton fibers and polyester from textile waste. J Clean Prod 2020;254:120078. https://doi.org/10.1016/j.jclepro.2020.120078.

[32] Patnaik S, Kumar S, Panda AK. Kinetics of thermal degradation of non-woven plastics: model-free kinetic approach. ChemistrySelect 2019;4:8054–60. https://doi.org/10.1002/slct.201901114.

[33] Deng N, feng ZY, Wang Y. Thermogravimetric analysis and kinetic study on pyrolysis of representative medical waste composition. Waste Manag 2008;28:1572–80. https://doi.org/10.1016/j.wasman.2007.05.024.

[34] Nawaz A, Kumar P. Optimization of process parameters of Lagerstroemia speciosa seed hull pyrolysis using a combined approach of response surface methodology (RSM) and artificial neural network (ANN) for renewable fuel production. Bioresour Technol Rep 2022;18:101110. https://doi.org/10.1016/J.BITEB.2022.101110.

[35] Nawaz A, Kumar P. Pyrolysis of mustard straw: evaluation of optimum process parameters, kinetic and thermodynamic study. Bioresour Technol 2021;340:125722. https://doi.org/10.1016/j.biortech.2021.125722.

[36] Vassilev SV, Baxter D, Andersen LK, Vassileva CG, Morgan TJ. An overview of the organic and inorganic phase composition of biomass. Fuel 2012;94:1–33. https://doi.org/10.1016/j.fuel.2011.09.030.

[37] Schwartz NR, Paulsen AD, Blaise MJ, Wagner AL, Yelvington PE. Analysis of emissions from combusting pyrolysis products. Fuel 2020;274:117863. https://doi.org/10.1016/j.fuel.2020.117863.

[38] Nawaz A, Singh B, Kumar P. Efficient removal of Cr (VI) using raw and phosphoric acid modified sterculia alata nutshell. Indian Journal of Chemical Technology 2021;28:684–92.

[39] Nawaz A, Singh B, Kumar P. H_3PO_4-modified Lagerstroemia speciosa seed hull biochar for toxic Cr(VI) removal: isotherm, kinetics, and thermodynamic study. Biomass Convers Biorefinery 2021. https://doi.org/10.1007/s13399-021-01780-8.

[40] Furushima Y, Ota R, Ohkawa T. Isothermal thermogravimetric method using a fast scanning calorimeter and its application in the isothermal oxidation of nanogram-weight polypropylene. Thermochim Acta 2020;694:178804. https://doi.org/10.1016/j.tca.2020.178804.

[41] Yue Z, Vakili A, Wang J. Activated carbon fibers from meltblown isotropic pitch fiber webs for vapor phase adsorption of volatile organic compounds. Chem Eng J 2017;330:183–90. https://doi.org/10.1016/j.cej.2017.07.150.

[42] Aboulkas A, El harfi K, El Bouadili A. Thermal degradation behaviors of polyethylene and polypropylene. Part I: pyrolysis kinetics and mechanisms. Energy Convers Manag 2010;51:1363–9. https://doi.org/10.1016/j.enconman.2009.12.017.

[43] Niemczyk A, Dziubek K, Sacher-Majewska B, Czaja K, Czech-Polak J, Oliwa R, et al. Thermal stability and flame retardancy of polypropylene composites containing siloxane-silsesquioxane resins. Polymers 2018;10. https://doi.org/10.3390/polym10091019.

[44] Kim SS, Kim S. Pyrolysis characteristics of polystyrene and polypropylene in a stirred batch reactor. Chem Eng J 2004;98:53–60. https://doi.org/10.1016/S1385-8947(03)00184-0.

[45] Yousef S, Eimontas J, Striūgas N, Tatariants M, Abdelnaby MA, Tuckute S, et al. A sustainable bioenergy conversion strategy for textile waste with self-catalysts using mini-pyrolysis plant. Energy Convers Manag 2019;196:688–704. https://doi.org/10.1016/j.enconman.2019.06.050.

[46] Mishra RK, Mohanty K. Pyrolysis of Manilkara zapota seeds over ZSM-5 to produce high-quality bio-oil and chemicals. Fuel 2020;280:118594. https://doi.org/10.1016/j.fuel.2020.118594.

[47] Zhang J, Nolte MW, Shanks BH. Investigation of primary reactions and secondary effects from the pyrolysis of different celluloses. ACS Sustain Chem Eng 2014;2(12):2820–30. https://doi.org/10.1021/sc500592v.

[48] Patwardhan PR, Dalluge DL, Shanks BH, Brown RC. Distinguishing primary and secondary reactions of cellulose pyrolysis. Bioresour Technol 2011;102:5265–9. https://doi.org/10.1016/J.BIORTECH.2011.02.018.

[49] Zhou Q, Liu Q, Shi L, Yan Y, Liu Z. Behaviors of coking and radicals during reaction of volatiles generated from fixed-bed pyrolysis of a lignite and a subbituminous coal. Fuel Process Technol 2017;161:304–10. https://doi.org/10.1016/J.FUPROC.2017.01.040.

[50] Liu Z, Guo X, Shi L, He W, Wu J, Liu Q, et al. Reaction of volatiles – a crucial step in pyrolysis of coals. Fuel 2015;154:361–9. https://doi.org/10.1016/J.FUEL.2015.04.006.

[51] Akhtar J, Saidina Amin N. A review on operating parameters for optimum liquid oil yield in biomass pyrolysis. Renew Sustain Energy Rev 2012;16:5101–9. https://doi.org/10.1016/J.RSER.2012.05.033.
[52] Nawaz A, Mishra RK, Sabbarwal S, Kumar P. Studies of physicochemical characterization and pyrolysis behavior of low-value waste biomass using Thermogravimetric analyzer: evaluation of kinetic and thermodynamic parameters. Bioresour Technol Rep 2021;16:100858. https://doi.org/10.1016/J.BITEB.2021.100858.
[53] Nawaz A, Kumar P. Elucidating the bioenergy potential of raw, hydrothermally carbonized and torrefied waste Arundo donax biomass in terms of physicochemical characterization, kinetic and thermodynamic parameters. Renew Energy 2022;187:844–56. https://doi.org/10.1016/j.renene.2022.01.102.
[54] Miranda R, Sosa_Blanco C, Bustos-Martínez D, Vasile C. Pyrolysis of textile wastes: I. Kinetics and yields. J Anal Appl Pyrolysis 2007;80:489–95. https://doi.org/10.1016/j.jaap.2007.03.008.
[55] Zhu F, Feng Q, Xu Y, Liu R, Li K. Kinetics of pyrolysis of ramie fabric wastes from thermogravimetric data. J Therm Anal Calorim 2015;119:651–7. https://doi.org/10.1007/s10973-014-4179-3.
[56] Yousef S, Eimontas J, Striūgas N, Abdelnaby MA. A new strategy for butanol extraction from COVID-19 mask using catalytic pyrolysis process over ZSM-5 zeolite catalyst and its kinetic behavior. Thermochim Acta 2022;711:179198. https://doi.org/10.1016/J.TCA.2022.179198.
[57] Liu H, Wang C, Zhang J, Zhao W, Fan M. Pyrolysis Kinetics and thermodynamics of typical plastic waste. Energy Fuels 2020;34:2385–90. https://doi.org/10.1021/acs.energyfuels.9b04152.
[58] Zou H, Evrendilek F, Liu J, Buyukada M. Combustion behaviors of pileus and stipe parts of Lentinus edodes using thermogravimetric-mass spectrometry and fourier transform infrared spectroscopy analyses: thermal conversion, kinetic, thermodynamic, gas emission and optimization analyses. Bioresour Technol 2019;288:121481. https://doi.org/10.1016/j.biortech.2019.121481.
[59] Zhang J, Liu J, Evrendilek F, Xie W, Kuo J, Zhang X, et al. Kinetics, thermodynamics, gas evolution and empirical optimization of cattle manure combustion in air and oxy-fuel atmospheres. Appl Therm Eng 2019;149:119–31. https://doi.org/10.1016/j.applthermaleng.2018.12.010.
[60] Vyazovkin S, Burnham AK, Criado JM, Pérez-Maqueda LA, Popescu C, Sbirrazzuoli N. ICTAC kinetics committee recommendations for performing kinetic computations on thermal analysis data. Thermochim Acta 2011;520:1–19. https://doi.org/10.1016/j.tca.2011.03.034.
[61] Cai J, Rahman MM, Zhang S, Sarker M, Zhang X, Zhang Y, et al. Review on aging of bio-oil from biomass pyrolysis and strategy to slowing aging. Energy Fuels 2021;35:11665–92. https://doi.org/10.1021/acs.energyfuels.1c01214.
[62] Kass MD, Armstrong BL, Kaul BC, Connatser RM, Lewis S, Keiser JR, et al. Stability, combustion, and compatibility of high-viscosity heavy fuel oil blends with a fast pyrolysis bio-oil. Energy Fuels 2020;34:8403–13. https://doi.org/10.1021/acs.energyfuels.0c00721.
[63] Yousef S, Eimontas J, Stasiulaitiene I, Zakarauskas K, Striūgas N. Pyrolysis of all layers of surgical mask waste as a mixture and its life-cycle assessment. Sustain Prod Consum 2022;32:519–31. https://doi.org/10.1016/J.SPC.2022.05.011.
[64] Gautam R, Vinu R. Non-catalytic fast pyrolysis and catalytic fast pyrolysis of nannochloropsis oculata using Co-Mo/γ-Al_2O_3 catalyst for valuable chemicals. Algal Res 2018;34:12–24. https://doi.org/10.1016/J.ALGAL.2018.06.024.
[65] Song Y, Hu J, Evrendilek F, Buyukada M, Liang G, Huang W, et al. Reaction mechanisms and product patterns of Pteris vittata pyrolysis for cleaner energy. Renew Energy 2021;167:600–12. https://doi.org/10.1016/J.RENENE.2020.11.122.